Acta Materialia 296 (2025) 121279

Contents lists available at ScienceDirect

Acta Materialia

journal homepage: www.elsevier.com/locate/actamat

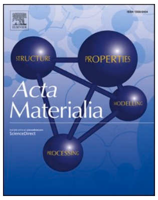

Full length article

Complete structural studies of long period stacking ordered (LPSO) phases in the Y-Ni-Mg system by 3D electron diffraction

Pavlo Solokha [a,*], Riccardo Freccero [a], Mauro Gemmi [b], Iryna Andrusenko [b,c], Paola Parlanti [b], Enrico Mugnaioli [c,d], Gwladys Steciuk [e], Lukas Palatinus [e], Serena De Negri [a]

[a] Dipartimento di Chimica e Chimica Industriale, Università degli Studi di Genova, via Dodecaneso 31, 16146 Genova, Italy
[b] Istituto Italiano di Tecnologia, Center for Materials Interfaces, Electron Crystallography, Viale Rinaldo Piaggio 34, 56025 Pontedera (PI), Italy
[c] Center for Instrumentation Sharing of the University of Pisa (CISUP), University of Pisa, Lungarno Pacinotti 43/44, 56426 Pisa, Italy
[d] Department of Earth Sciences, University of Pisa, Via S. Maria 53, 56126 Pisa, Italy
[e] Department of Structure Analysis, Institute of Physics of the CAS, Na Slovance 2 Prague 8, 18221 Prague, Czechia

ARTICLE INFO

Keywords:
Magnesium alloys
Intermetallic compounds (IMCs)
Electron diffraction pattern
Structural modulation
Phase diagrams

ABSTRACT

The crystal structures of three Y-Ni-Mg LPSO phases were directly solved from diffraction data of X-rays ($(Mg@Y_8Ni_6)Mg_{18}$, $tI66\text{-}Nd_{8+x}Ru_6Mg_{19\text{-}x}$) and electrons ($(Mg@Y_8Ni_6)_{16}Mg_{505}$ and $(Mg@Y_8Ni_6)_3Mg_{154}$)). The latter two are modulated structures described in 6D(*Fm*-3*m*(α00)000(0α0)000(00α)000, $\mathbf{q1} = 0.441(6)\ \mathbf{a}^*$, $\mathbf{q2} = 0.441(6)\ \mathbf{b}^*$, and $\mathbf{q3} = 0.441(6)\ \mathbf{c}^*$) and 5D (*R*-3*c*(αα0)00(-2α,α0)00, $\mathbf{q_1} = 0.1457(7)\ \mathbf{a}^* + 0.1457(7)\ \mathbf{b}^*$, $\mathbf{q_2} = -0.2915(7)\ \mathbf{a}^* + 0.1457(7)\ \mathbf{b}^*$) superspaces, respectively. The 3D electron diffraction was applied here for the first time to LPSO compounds, turning out to be the only method successfully overcoming the numerous problems hampering their complete structure solution.

The structural analysis of these compounds resulted in a generalized description of Y-Ni-Mg LPSO phases in terms of $Mg@Y_8Ni_6$ clusters more or less densely distributed in a Mg matrix, justifying the proposed formulas. LPSO classification based on the layer stacking modes is proposed, leading to *fcc* (*c*-type) and hybrid *fcc/hcp* (*(h)*$_n$*cc*-type) subfamilies, the former being identified in this work and including $(Mg@Y_8Ni_6)Mg_{18}$ as well as $(Mg@Y_8Ni_6)_{16}Mg_{505}$.

The inter-clusters coordination in form of distorted anticuboctahedra or cuboctahedra is a further fingerprint of membership in either family. Increasing the magnesium content, the $Mg@Y_8Ni_6$ units tend to form aggregates at characteristic inter-cluster distances, the distribution of which is at the origin of the structural modulation.

1. Introduction

Long period stacking ordered (LPSO) phases represent a hot topic in the Mg-based alloys research [1], as witnessed by the quick growth of related publications. Starting from 2002[2], more than 1300 papers have appeared in peer-reviewed international journals (see Fig. 1a).

LPSOs are typically ternary phases where magnesium is the principal component (> 75 at. %), alloyed with a rare earth metal (*RE*, commonly Y and Gd) and Co, Ni, Cu, Zn or Al (*T* component) [3], as shown in Fig. 1b. The LPSO-containing lightweight alloys show excellent properties, such as deformability, high strength and stiffness, thermal stability, corrosion resistance, etc [3–7]. Therefore, the large majority of investigations focus on their synthesis, treatments and mechanical/-functional characterization, often in a direct connection with practical applications [8–14].

On the other hand, despite numerous efforts, the structural characterization of these intermetallics has remained fragmentary and incomplete. This is a consequence of both their intrinsic structural complexity and the unavoidable experimental difficulties, among which:

- the existence of many LPSO phases with similar composition and structure, often coexisting in the synthesized ternary samples;
- the occurrence of complex multiphase microstructures, not achieving thermodynamic equilibrium even after prolonged annealing (the maximum temperature of treatments is limited by the relatively low melting point);

---

* Corresponding author.
E-mail address: pavlo.solokha@unige.it (P. Solokha).

https://doi.org/10.1016/j.actamat.2025.121279
Received 11 February 2025; Received in revised form 18 June 2025; Accepted 19 June 2025

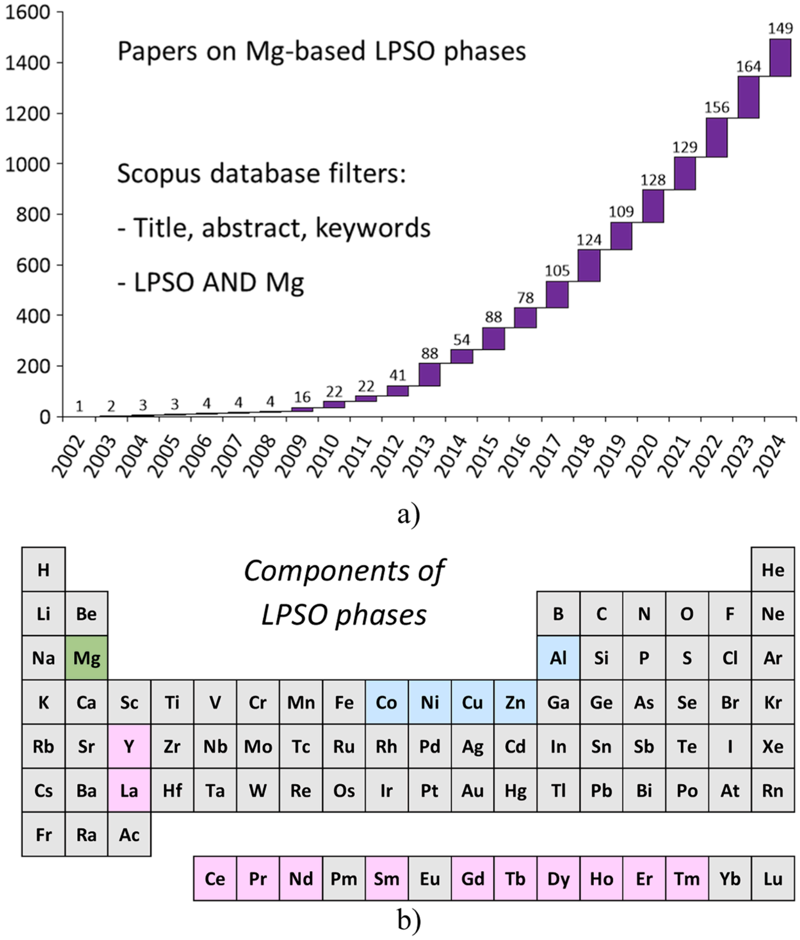

Fig. 1. a) Publications on magnesium LPSO phases from their discovery up to 2024; b) elements involved in RE-T-Mg LPSO phases (source: Scopus database[15]).

- LPSO mechanical properties, such as ductility, that make it almost impossible to grind samples to obtain powders and/or to extract single crystals of proper size and quality.

All these problems hampered the application of classical methods for crystal structure determination, such as powder and single crystal X-ray diffraction (XRD). To overcome them, transmission electron microscopy (TEM) techniques have been used for crystallographic purposes, including oriented-pattern electron diffraction, convergent-beam electron diffraction (CBED), and high-angle annular dark-field scanning-transmission electron microscopy (HAADF-STEM) [2,16–19]. The main advantage of these approaches is the possibility to analyse very small single-phase areas and to get information about periodicity and unit cell parameters. However, 3D structural models are not easy to extract from 2D data. As a result of this limitation, the LPSO phases were modelled as a stacking of compact layers along one direction (corresponding to *c*-axis in most cases). According to this representation, the Ramsdell's notation was naturally chosen to identify each phase: it consists of a symbol including the number of layers in the unit cell followed by the letter H, R or C to indicate the lattice type [20]. The most common LPSO structures are then 24H, 18R, 14H and 10H [16,18,19]. This description has the merit of highlighting a common architecture for the LPSO family of compounds, but it suffers from severe drawbacks. In the Ramsdell's notation, there is no indication about the exact stacking sequence of layers. In principle, this information can be extracted from the TEM characterization, but differently oriented high-resolution and good quality images are necessary, which is often a tricky task to accomplish. The overall composition evidently depends on the composition of each single layer, which is not quantitatively "measurable" by TEM techniques. Therefore, it is difficult to match qualitative models with the overall phase composition, measured, for example, by SEM-EDXS and confusion arises both in the identification of LPSO phases (number/-composition/structure) in a given system and in establishing correspondences between analogue phases in different systems.

Another aspect to be mentioned is that, for the majority of LPSO phases, the available structural information is presented in the form of Ramsdell's notation without a complete set of atomic positions, and then cannot be uploaded in the most widespread crystallographic databases, e.g. ICSD [21] and Pearson's Crystal Data [22]. This prevents a rational organization and efficient sharing of the scientific results obtained by different research groups.

Most of the discussed problems are associated with the poor information available from 2D characterization methods. A possible way to overcome these limitations is the generation of theoretical 3D models that can be compared with and validated by experimental data. This task was addressed in some works [17–19,23,24] where complete structural models were proposed for selected Y-Zn-Mg, Gd-Al-Mg and Y-Ni-Mg LPSO phases. The presence of RE_8T_6 clusters embedded in a Mg matrix was assumed for the construction of the models. Despite the impressive, not automatable work necessary to achieve these results, the obtained models partially depend upon unverifiable assumptions and are not unambiguous.

Hence, how to get complete, trustable structural models for LPSO with no guesses? Until some years ago, there were probably no alternatives to the abovementioned 2D approaches. Only recently, the 3D electron diffraction (3D ED) method has become available for a large number of applications at the micro and nano scale [25]. This method is based on a systematic acquisition of electron diffraction data while the

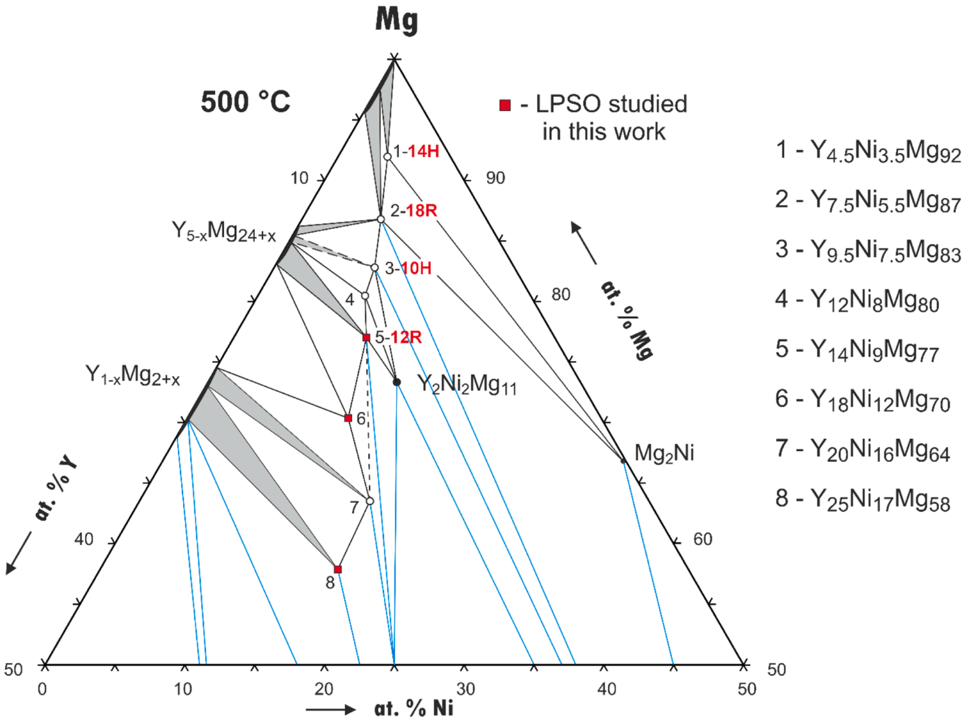

Fig. 2. Partial Y-Ni-Mg isothermal section based on our experimental data (extended two phase regions are filled in grey). Uncertain equilibria are dotted. Blue lines correspond to equilibria converging versus Mg-poorer ternary phases. LPSO phases are numbered from 1 to 8; where possible, the correspondence with structural models reported in the literature (Ramsdell's notation) was indicated.

sample is tilted, and allows for the 3D atomic structure determination of nano-dimensioned crystalline materials [25–30]. At present, the number of intermetallics elucidated by 3D ED is very moderate [31–33] and we targeted LPSO phases as good candidates to be tested by this method. In this regard, we used focused ion beam-scanning electron microscopy (FIB-SEM) [34] to selectively pick up nanocrystals of interest from ductile, multiphase, microstructurally complex LPSO alloys.

In this work we present the results of a combined 3D ED/XRD study, by which the complete crystal structures of three Y-Ni-Mg LPSO phases were obtained and elucidated for the first time. The deeper analysis of the obtained models led to a more general view of the architecture and the definition of LPSO phases in this specific system.

2. Experimental section

2.1. Synthesis and SEM/EDXS characterization

Samples used for structure solutions of novel compounds were prepared starting from elements with purities higher than 99.9 mass %. The synthesis route was slightly adapted from that proposed by Shtender et al [35]: precursor Y-Ni binary alloys of $Y_{60}Ni_{40}$ and $Y_{64}Ni_{36}$ nominal compositions were prepared by arc melting and manually ground in a mortar. Their powders were mixed with magnesium turnings in stoichiometric amounts, to get $Y_{30}Ni_{20}Mg_{50}$ and $Y_{16}Ni_9Mg_{75}$ nominal compositions, respectively and a total mass of about 0.5 g each.

Subsequently, the mixtures were pressed in pellets, put in arc-sealed Ta crucibles, enclosed in silica tubes and sealed under inert atmosphere. The following thermal cycle was then applied inside a resistance furnace: 500°C → (0.2°C/min) → 800°C (5 min) → (-0.2°C/min) → 500°C (annealing for 250 h). After the annealing time, the furnace was switched off and samples left inside to reach room temperature.

Samples used for phase equilibria studies (see Fig. S1) were prepared by induction melting of the starting metals in stoichiometric amounts inside arc-sealed Ta crucibles and subsequent annealing at 500°C for at least one month.

For SEM/EDXS characterization, samples were embedded in a phenolic resin with carbon filler, smoothed by SiC abrasive papers and polished by diamond pastes with particle size decreasing from 6 to 1 µm. A Zeiss Evo 40 Scanning Electron Microscope (SEM) equipped with a Dispersive X-ray Spectroscopy (EDXS) system (INCA X-ACT) operated by the INCA Energy software (Oxford Instruments, Analytical Ltd., Bucks, U.K.) was used for microstructure characterization and qualitative and quantitative analyses (see Tables S1 and S2 and Fig. S2).

2.2. Single crystal X-ray diffraction

A good quality single crystal of the $Y_8Ni_6Mg_{19}$ compound was selected under a light microscope from the mechanically crushed $Y_{30}Ni_{20}Mg_{50}$ sample and glued on a glass fibre.

The X-ray diffraction measurement was performed at room conditions on a three-circle Bruker D8 QUEST diffractometer equipped by a PHOTON III 14 photon counting detector, using the graphite monochromatized Mo Kα radiation. Data collection strategies, consisting of three ω- and two φ-scans, were chosen with the aid of the APEX4 software [36], guaranteeing good data completeness, redundancy, and resolution. Data were collected up to ~ 36° in θ (achieving a resolution of ca. 0.6 Å) with exposures of 30 s per frame. Data were successfully integrated, reduced, and corrected (Lorentz, polarization, and absorption effects) inside APEX4. The crystal structure was solved and refined with the aid of SHELXTL [37].

2.3. TEM and 3D electron diffraction

Two lamellae (<100 nm thickness) from LPSO-6 and LPSO-5 were prepared using a Helios NanoLab 600i dual beam focused ion beam-SEM (FIB-SEM) (ThermoFisher), equipped with an Omniprobe micromanipulator (Oxford Instruments) for TEM sample lift-out. Sections were placed on FIB/TEM Cu-grid (EMS) for TEM analysis. High-resolution (HR) TEM images and oriented selected area electron diffraction (SAED) patterns were collected with a JEOL JEM F200 Multipurpose

Table 1
Selected crystallographic data and structure refinement parameters for the single crystals studied in this work.

Compound	$(Mg@Y_8Ni_6)Mg_{18}$ LPSO-8	$(Mg@Y_8Ni_6)_{16}Mg_{505}$ LPSO-6	$(Mg@Y_8Ni_6)_3Mg_{154}$ LPSO-5
EDXS composition	$Y_{26.0}Ni_{17.8}Mg_{56.2}$	$Y_{17.8}Ni_{12.4}Mg_{69.8}$	$Y_{13.5}Ni_{9.3}Mg_{77.2}$
Radiation	X-ray, Mo Kα	Electrons, 120 keV ($\lambda = 0.033492$)	
Depositing CSD-code	2272476	2410585	2410588
Formula weight (g/mol)	1525.43	29677.11	7006.05
Space group	*I*4/*mmm* (139)	*Fmm*2 (42)*	*R*-3*c* (167)*
Pearson symbol, Z	*tI*66, 2	*oF*2980, 4	*hR*1194, 6
Prototype	$Nd_{8+x}Ru_6Mg_{19-x}$	own	own
a, Å	9.0750(1)	41.6857(10)	22.3290(16)
b, Å	9.0750(1)	41.6857(10)	22.3290(16)
c, Å	18.0081(5)	41.6857(10)	62.780(15)
V, $Å^3$	1483.07(5)	72437(3)	27107(7)
Calc. density ($g \cdot cm^{-3}$)	3.42	2.72	2.57
Abs. coeff. (μ, mm^{-1})	19.55	none	none
Theta range (°)	$3.2 \leq \theta \leq 36.4$	$0.09 \leq \theta \leq 1.34$	$0.08 \leq \theta \leq 1.3$
sinθ/λ ($Å^{-1}$)	$0.79 \leq \sin\theta/\lambda \leq 8.37$	$0.047 \leq \sin\theta/\lambda \leq 0.7$	$0.042 \leq \sin\theta/\lambda \leq 0.68$
Index ranges *h, k, l*	$-15 \leq h \leq 15$	$-58 \leq h \leq 58$	$-28 \leq h \leq 29$
	$-13 \leq k \leq 15$	$-55 \leq k \leq 58$	$-29 \leq k \leq 29$
	$-30 \leq l \leq 30$	$-58 \leq l \leq 58$	$-84 \leq l \leq 84$
Nobs/Nall	1087/25805 (2σ(I))	966/19965 (3σ(I))	637/4942 (3σ(I))
Data/parameters	1087/34	966/47	637/76
GOFobs/all	1.06	0.0248/0.0075	0.0431/0.0180
R_{int}/R_{sym}	0.0844/0.0333		
*R*1/*wR*2 ($I > 2\sigma(I)$), (R_{obs}/wR_{obs}) ($I > 3\sigma(I)$)**	0.0373/0.1018	0.2211/0.2585	0.3430/0.3243
*R*1/*wR*2 (all data) (R_{all}/wR_{all})**	0.0671/0.1180	0.5984/0.3100	0.6862/0.3741
Max diff. peak and hole ($e^-/Å^3$)	4.811/ -1.034	2.03/-1.45	4.36/-2.74

* Commensurate three-dimensional average model

** 3D ED data are refined on *F*(obs)

TEM, working at 200 kV and equipped with a Schottky field emission gun (FEG). HRTEM images were acquired with a Gatan Rio16 CMOS camera (4k x 4k pixels) and analysed by DigitalMicrograph software, including fast Fourier transform (FFT) and image filtering. SAED patterns were acquired with an ASI Cheetah hybrid-pixel electron detector (512 × 512 pixels) and analysed by ImageJ software [38].

HAADF-STEM imaging (Fig. S3) and 3D ED data were recorded with a Zeiss Libra 120 TEM operating at 120 kV and equipped with a LaB_6 source. 3D ED was performed in STEM mode after defocusing the beam in order to have a pseudo-parallel illumination on the sample, as described in Lanza et al. [39]. ED patterns were collected in Köhler parallel illumination with a beam size of about 150 nm in diameter, obtained using a 5 μm C2 condenser aperture. Data were recorded on a single-electron ASI MEDIPIX detector [40]. 3D ED data collections were performed in stepwise modes with the beam precession performed using a Nanomegas Digistar P1000 device [41] (tilt step = 1°, precession angle = 1°). The 3D ED data sets covered tilt ranges of 110° (LPSO-5) and 120° (LPSO-6). After each tilt, a diffraction pattern was acquired, and the crystal position was tracked by defocused STEM imaging. Camera length of 180 mm was used, allowing for a resolution in real space of about 0.7 Å. ED data were energy filtered by an in-column omega filter [42]. 3D ED data reduction was performed with the program PETS2 [43–45] which can account for modulation.

3. Results and discussion

3.1. Phase equilibria in the Y-Ni-Mg system

The Y-Ni-Mg system has been extensively studied for about 20 years, covering different aspects. The first reported compounds, Y_2Ni_2Mg, YNi_4Mg and YNi_9Mg_2, date back to 2000 [22]. About ten years later, the Mg-richest LPSO phase (14H) was discovered [8] and subsequently some others (18R, 10H, 12R) were investigated [10,24,46,47]. Recently, YNiMg, $Y_4Ni_2Mg_3$ and $Y_2Ni_2Mg_{11}$, were structurally elucidated [35]. In the same period, several works on phase equilibria were published, based on experimental data [48–50] as well as on thermodynamic optimizations [51,52]. In these papers, numerous new phases were reported, based only on microstructure/compositional data, without any structural elucidation. Therefore, fundamental knowledge about the Y-Ni-Mg system remains incomplete and chaotic. We have been studied this system for over ten years, facing numerous experimental obstacles and only now we are confident to present sound results on some aspects of this topic.

The isothermal section at 500°C of the Mg-corner of the studied phase diagram is shown in Fig. 2, as determined from the synthesis and characterization of more than 30 samples; details on their SEM/EDXS data are reported in the SI file (see Tables S1 and S2). Based on phase analysis, nine ternary compounds were found, one corresponding to $Y_2Ni_2Mg_{11}$ [35], the others all located close to the compositional line with Y/Ni ratio equal to 4/3. Their EDXS average compositions, each obtained from several different samples, are listed in Fig. 2. Among them, there are four compounds already reported in the literature as LPSO phases (indicated as 14H, 18R, 10H and 12R with decreasing Mg content) and four new compounds possibly expanding this family down to about 57 at. % Mg (LPSO-8). The compounds of interest are in equilibrium with each other, starting from magnesium and following the compositional trend. A major part of tie-lines connects them to Y-Mg or $NiMg_2$ binaries. Some equilibria towards Mg-poorer ternary phases (not addressed here) were observed. In the next paragraphs, a detailed structural study of three LPSO phases (5, 6 and 8) is presented.

3.2. Crystal structure of the novel Y-Ni-Mg phases

Details of data collection and structure refinement for the studied compounds are summarized in Table 1 together with selected crystal data; standardized atomic coordinates and equivalent displacement parameters are listed in Tables S3–S5. The corresponding CIF files, available as supplementary material, were deposited at the Cambridge Database.

3.2.1. $(Mg@Y_8Ni_6)Mg_{18}$ (LPSO-8)

The diffraction pattern of this phase shows a body-centred tetragonal symmetry with no additional systematic extinctions. The best structural model was found using the intrinsic phasing method in the *I*4/*mmm* space group (N. 139). The unit cell, containing 2 formula units of $Y_8Ni_6Mg_{19}$ composition, counts 66 atoms, distributed among 1 Wyckoff

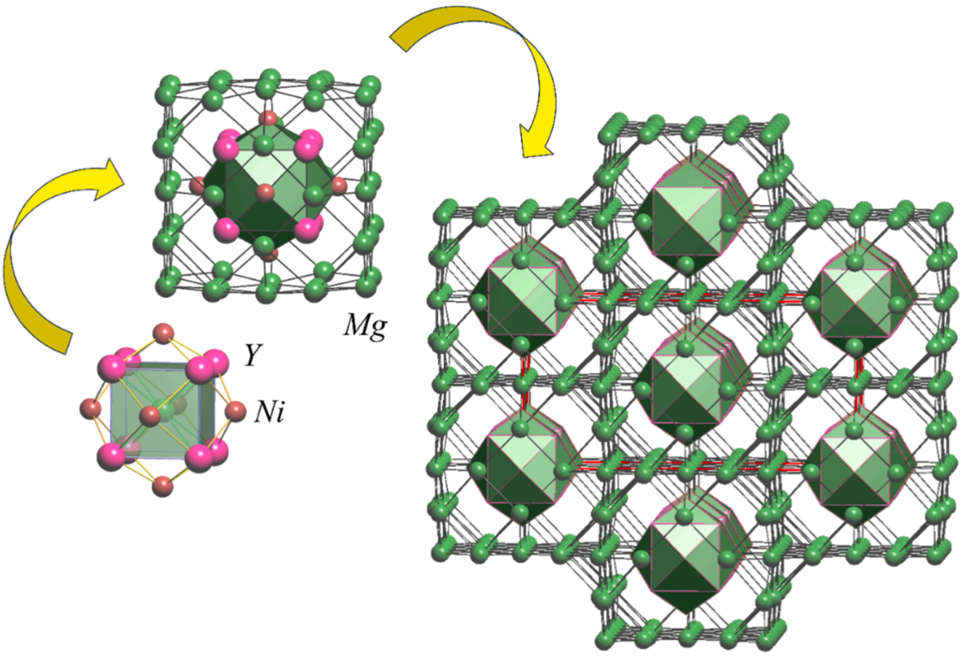

Fig. 3. Crystal structure of $Y_8Ni_6Mg_{19}$ as built by Mg@Y_8Ni_6 clusters embedded within the cages of an Mg framework with face-centred cubic topology. For the sake of clarity, Y and Ni atoms were hidden in the right part.

Table 2
Statistics of 3D ED data using the superspace formalism and transformation into supercells for LPSO-6 and LPSO-5.

	LPSO-6	LPSO-5
Superspace formalism	(3+3)D	(3+2)D
system	cubic	trigonal
a (Å)	4.6317(1)	3.1899(16)
b (Å)	4.6317(1)	3.1899(16)
c (Å)	4.6317(1)	62.780(15)
V (Å^3)	99.36	553.2
modulation wave vectors	$\mathbf{q1} = 0.441(6)\ \mathbf{a}^*$ $\mathbf{q2} = 0.441(6)\ \mathbf{b}^*$ $\mathbf{q3} = 0.441(6)\ \mathbf{c}^*$	$\mathbf{q1} = 0.1457(7)\mathbf{a}^* + 0.1457(7)\ \mathbf{b}^*$ $\mathbf{q2} = -0.2914(7)\mathbf{a}^* + 0.1457(7)\ \mathbf{b}^*$
Modulation component α	$\alpha \approx 4/9$	$\alpha \approx 1/7$ (= 0.1429)
modulation type	incommensurate	incommensurate
superspace group	*Fm*-3*m*(α00)000(0α0)000(00α)000	*R*-3*c*(αα0)00(-2α,α0)00
Index ranges	$-7 \le h \le 7$ $-7 \le k \le 7$ $-7 \le l \le 7$ $-2 \le m \le 2$ $-2 \le n \le 2$ $-2 \le p \le 2$	$-4 \le h \le 5$ $-4 \le k \le 4$ $-84 \le l \le 84$ $-2 \le m \le 2$ $-2 \le n \le 2$
Completeness for θmax	99.69 %	90.00 %
Rint(obs)/Rint(all)	0.2567/0.3248	0.3019/0.4135
Nobs/Nall (main, satellites)	(0,0): 15/16 ±(1,0,0): 40/60 ±(2,0,0): 17/59 ±(1,1,0): 43/92 ±(2,1,0): 28/153 ±(1,1,1): 24/73 ±(2,2,0): 3/93 ±(2,1,1): 15/165	(0,0): 106/165 ±(1,0): 331/918 ±(2,0): 61/911 ±(1,-1): 125/912 ±(2,-1): 17/1368 ±(2,-2): 14/685
supercell transformation	9*a* x 9*b* x 9*c*	7*a* x 7*b* x *c*
t_0, u_0, v_0	1/2, 1/4, 0	0, -, 0
Space group (3D)	*Fmm*2	*R*-3*c*

site of Y, 2 sites of Ni and 5 of Mg. The isotropic refinement resulted in good isotropic displacement parameters for all the species. The possibility of a statistical mixture/partial occupation scenario was checked for each Wyckoff site, giving no improvements. The final anisotropic full-matrix least-squares refinements of the stoichiometric model converged to good residuals.

This phase is isostructural with the $RE_{8+x}Ru_6Mg_{19-x}$ compounds (*RE* = Nd, Sm, Gd, Tb) [53,54], being the fifth representative of this family (see structural data listed in Table S3). The composition of the stoichiometric model is in a good agreement with the EDXS composition measured on several samples.

The 4:3 Y/Ni ratio places $Y_8Ni_6Mg_{19}$ on the compositional line typical of the already known LPSO phases, even with a significantly lower magnesium content. The structure analysis, however, confirms the presence of Mg-centered Y_8Ni_6 clusters, where Y atoms form a regular cube, and Ni atoms are arranged on the vertices of an octahedron (see Fig. 3). The distances between the central Mg and Y species are 3.16 Å, which is close to their atomic radii sum. The Mg–Ni contacts are somewhat longer, with values of 3.03–3.05 Å. The Mg@Y_8Ni_6 clusters were then considered as the fundamental building blocks: they are encapsulated inside Mg cages forming units with recognizable *fcc* topology (see Fig. 3) where Y and Ni atoms are somewhat displaced with respect to ideal positions due to the different sizes of these species compared to Mg. The overall crystal space could be represented as an infinite regular arrangement of the described units.

3.2.2. (Mg@Y_8Ni_6)$_{16}$Mg$_{505}$ (LPSO-6) and (Mg@Y_8Ni_6)$_3$Mg$_{154}$ (LPSO-5)

The analysis of 3D ED patterns showed that both title compounds are modulated (see Table 2 and text below) and the superspace formalism was used to properly index and integrate the reflections. The data reduction results in a *hkl(mnp)*-type of files assuming the kinematical approximation used in the structural solution and the kinematical refinement.

(Mg@Y_8Ni_6)$_{16}$Mg$_{505}$ (LPSO-6)

LPSO-6 was indexed in a *F*-centered cubic basic cell with parameter *a* = 4.6317(1) Å (Table 2 and Fig. 4). Three modulation vectors and indices up to 2 are needed to index all satellite reflections: **q1** = 0.441(6)

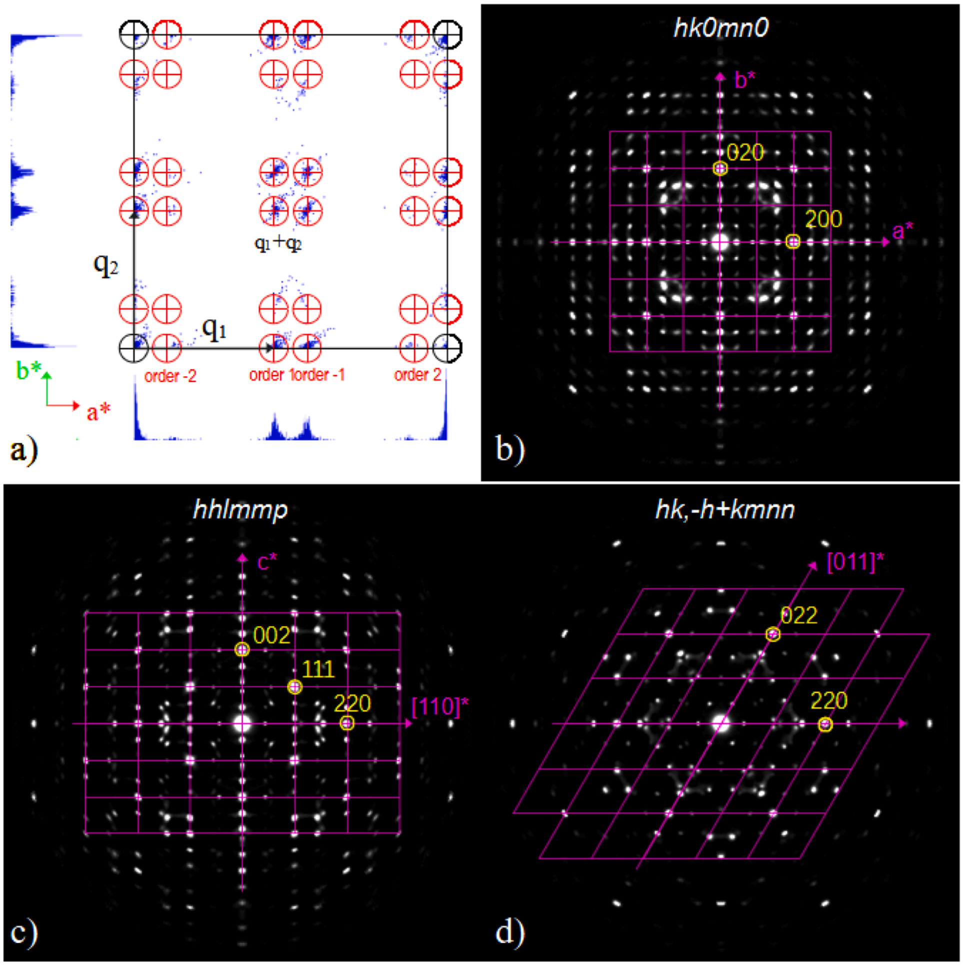

Fig. 4. Reciprocal space of LPSO-6 projected into one basic *F*-centered cubic unit cell (a = 4.6315(9) Å) where main reflections are marked in black and satellite reflections (marked in red) are described using three modulation wave vectors. a) Projection in b^*-c^* showing the satellite reflections up to 2nd order. b-d) Reciprocal sections of LPSO-6 representative of the *F*-centered cubic lattice in (3+3)D. The purple overlay represents the *F*-centered cubic basic cell.

a*, **q2** = 0.441(6) **b***, and **q3** = 0.441(6) **c*** with the modulation component α = 0.441(6) very close to a commensurate value 4/9 (Fig. 4). The analysis of reciprocal space sections indicate only extinction due to the *F* centering, and the first structure solution attempt in superflip [55,56] confirmed the superspace group $Fm\text{-}3m(\alpha00)000(0\alpha0)000(00\alpha)000$. The initial solution in the superspace formalism could not be interpreted properly in 6D due to the discontinuity in the atomic domains.

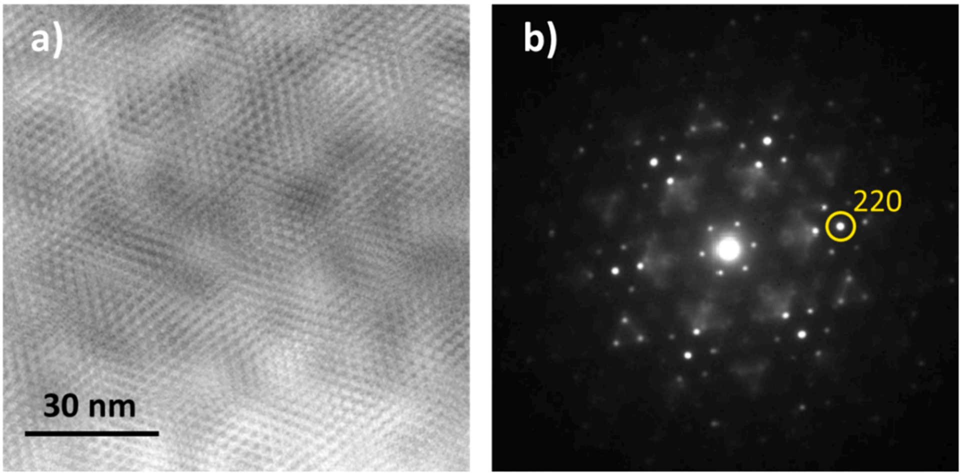

Fig. 5. Results of the TEM characterization of LPSO-6. (a) Filtered HRTEM image taken along [111], showing the pseudo-hexagonal periodicity of 1.6 Å, together with the long range non-periodic order represented by crossing features with different contrast. (b) SAED pattern along [111] showing the main pseudo-hexagonal periodicity, together with the satellite reflections and the diffuse scattering features.

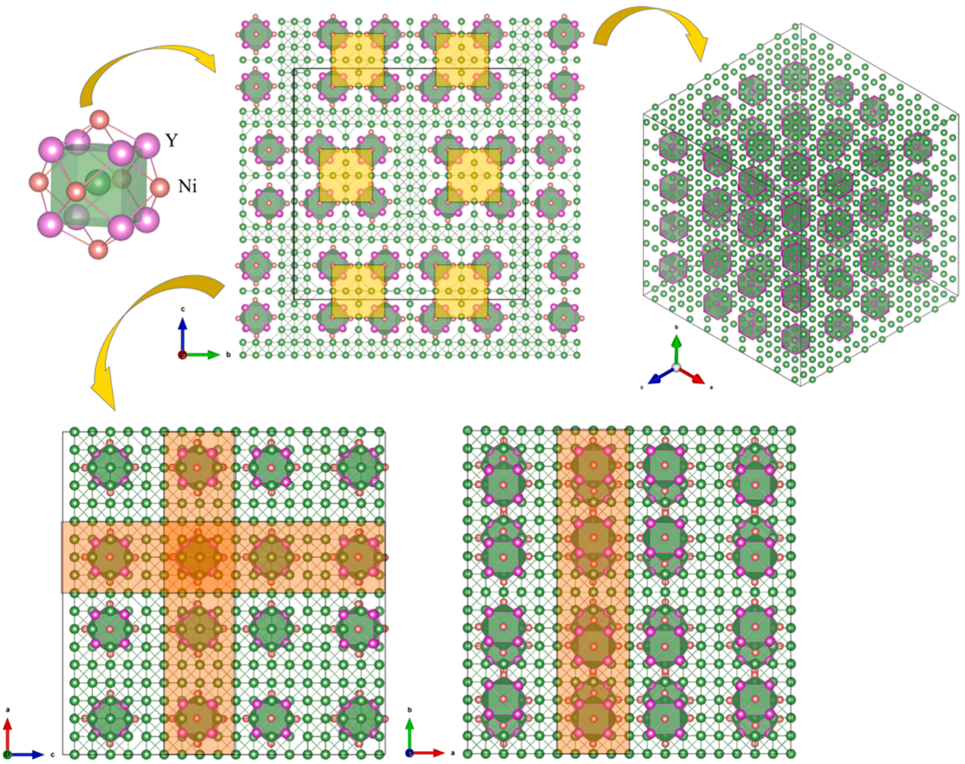

Fig. 6. LPSO-6 3D average model viewed as the evolution from a single $Mg@Y_8Ni_6$ cluster to the cluster distribution within a slab to the full structure projected along [010], [001] and [111]. Yellow squares highlight the distribution of clusters within a slab; orange rectangles highlight identical slabs in the different projections.

The initial solution contains one atomic site that describes Mg, Y and Ni species with a combination of displacive and occupational modulations. A second site, which was not initially found and only partially occupied, was later identified as the additional Mg at the center of the Y_8Ni_6 cluster. To tackle that issue, the structure solution was performed after transforming the reflections *hklmnp* of the (3+3)D formalism into a 9*a* x 9*b* x 9*c* pseudo-cubic supercell as the modulation component can be considered commensurate ($a = b = c = 41.6857(10)$ Å). In order to go from the superspace formalism to a supercell, t_0, u_0, v_0 sections must be defined [57]. Different combinations of values lead to different symmetries for the supercells. However, not all of them can properly describe the cluster ordering. Systematic tests have shown that the highest symmetry allowing an ordered arrangement of the clusters in the Mg matrix is *Fmm*2 for ($t_0 = ½$, $u_0 = ¼$, and $v_0 = 0$). Superflip was used to solve the LPSO-6 structure ab initio in the supercell in this symmetry, resulting in a 3D electrostatic potential map which was manually interpreted (Fig. S4). Based on the geometry, four individual Y_8Ni_6 clusters hosting Mg could be described as a moiety present in four positions. The refinement of 3D ED data was performed considering the kinematical approximation and six-fold pseudomerohedral twinning. Even though the data quality was good enough for the attempting dynamical refinement (Fig. S5), the size of the supercell ($V = 72{,}437(3)$ Å^3), the number of atoms in the asymmetric unit (185) and the six twin domains prevented the use of the dynamical theory of diffraction in the refinement due to computing limitations. To stabilize the refinement, Mg atoms were set to their initial cubic positions (derived from the 6D model), and only the cluster atoms were allowed to be shifted. One common isotropic displacement parameter was refined for all atoms. All positions were assumed fully occupied giving the formula $(Y_8Ni_6Mg)_{16}Mg_{505}$ with $Z = 4$. The refinement led to *R(obs)*/w*R(obs)* = 0.2211/0.2585, *R(all)*/w*R(all)* = 0.5984/0.3100 (see Table 1). LPSO-6 structure obtained from 3D ED is provided as a CIF file and was deposited in the CSD database under the deposition number 2410585. The data collection and refinement details are given Table 1 and Table 2, and the structural parameters in Table S4.

HRTEM images of LPSO-6 taken close to [111] show a pseudo-hexagonal symmetry, with lattice length of about 1.6 Å, corresponding to {220} planes of the non-modulated cell. After filtering-in only the reflections of Fast Fourier Transform (FFT) corresponding to this cell, we emphasize the occurrence of crossing features with different contrast, which reveal the longer range non-periodic character of the structure (Fig. 5a).

SAED patterns taken along the same direction confirm the occurrence of a pseudo-hexagonal modulation, corresponding to a periodicity of about 7.0–8.0 Å (b). Diffuse scattering is also present, with characteristic triangular and rhombic shapes (Fig. 5b). The pseudohexagonal periodicity fits well to the [111] direction of the basic cubic structural model (Fig. 6). The 1.6 Å periodicity corresponds to the average interplanar distance between Mg layers observed along this direction, while 7.0–8.0 Å corresponds to the average interplanar distance between $Mg@Y_8Ni_6$ cluster layers.

The fundamental building blocks of LPSO-6 are $Mg@Y_8Ni_6$ clusters identical to those in LPSO-8, which are distributed non periodically in the crystal, causing the observed modulation. In the 3D approximant model, the trace of it is the presence of undulating rows of clusters intersecting each other along [111] in the unit cell. Slabs of clusters can also be seen, highlighted in orange in two of the projections shown in Fig. 6; in each slab, clusters are gathered in squares about 9 Å apart. More features are discussed in the structural generalization paragraph.

$(Mg@Y_8Ni_6)_3Mg_{154}$ (LPSO-5)

The same structure solution strategy was used for LPSO-5. The reciprocal space was initially described using the superspace formalism in (3+2)D in a R_{obv} trigonal unit cell $a = 3.1899(16)$ Å, $c = 62.780(15)$ Å, where satellite reflections up to order 2 are described using the two modulation wave vectors $\mathbf{q_1} = 0.1457(7)\ \mathbf{a}^* + 0.1457(7)\ \mathbf{b}^*$, and $\mathbf{q_2} = -0.2915(7)\ \mathbf{a}^* + 0.1457(7)\ \mathbf{b}^*$. Sections of the reciprocal space indicate the superspace group *R*-3*c*(αα0)00(-2α,α0)00 with an incommensurate modulation $\alpha = 0.1457(7)$ (Fig. 7). For the same reasons as for LPSO-6, a

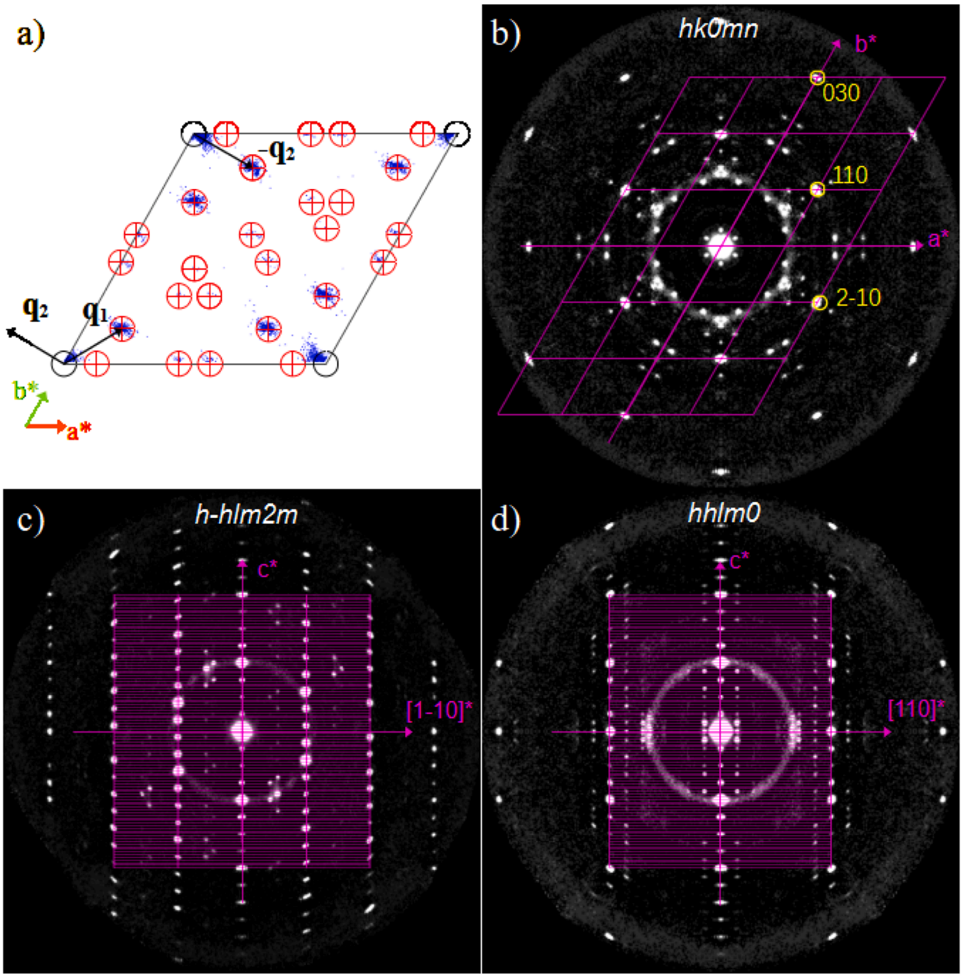

Fig. 7. Reciprocal space of LPSO-5 projected into one basic R_{obv}-centered trigonal unit cell (a = 3.1899(16) Å, c = 62.780(15) Å) where main reflections (marked in black) and satellite reflections (marked in red) are described using two modulation wave vectors. a) Projection of the reciprocal space into one basic reciprocal unit cell showing satellite reflections up to 2nd order. b-d) Reciprocal-space sections of LPSO-5 representative of the R_{obv} trigonal lattice in (3+2)D. The purple overlay represents the basic cell.

supercell had to be used to interpret the LPSO-5 model. As the modulation is incommensurate, an approximant supercell had to be used, obtained by considering $\alpha \approx 1/7$. The *hklmn* reflections were transformed into a 7*a* x 7*b* x *c* supercell (t_0 and $v_0 = 0$) with space group *R*-3*c*. The structure was solved ab-initio with Superflip and interpreted according to the geometry visible in the 3D electrostatic potential map (Fig. S6). The model has 35 atoms in the asymmetric unit cell with one cluster hosting Mg as for LPSO-6 and LPSO-8, and a composition $(Y_8Ni_6Mg)_3Mg_{154}$ for $Z = 6$. The refinement in the kinematical approximation yields *R(obs)/wR(obs)* = 0.3573/0.3419, *R(all)/wR(all)* = 0.6862/0.3741 for 894/4942 observed over all reflections. The quite high *R*-values can be explained by two main factors: the satellite reflections are weak and since they are located close to each other their proper integration in the reciprocal space is challenging, causing a significant error in their intensity estimation. On the other side, the high complexity of the structure and its intrinsic disorder, visible as a diffuse scattering in certain sections of the diffraction pattern, also give their worsening contribution. LPSO-5 structure obtained from 3D ED is provided as a CIF file and was deposited in the CSD database under the deposition number 2410588. The data collection and refinement details are given in Tables 1 and Table 2, and the structural parameters in Table S5.

HRTEM images of LPSO-5 taken along [010] direction show a layered structure with an interplanar distance of about 10–11 Å, corresponding to (006) planes in the non-modulated structure. These layers are interested by disorder features of intra- and inter-layer nature, like stacking faults and closure and kinking of layers (Fig. 8a–c). The related FFTs and SAED patterns (inset in Fig. 8a and Fig. 8d) show three relevant features: i) lines of strong reflections along *c** indicating a supercell with respect to the *hcp*-Mg cell; ii) a second line of reflections with interplanar distance of about 2.7 Å, corresponding to {-102} planes of the non-modulated structure; iii) two lines of weak reflections in between being a fingerprint of intrinsic structural modulation. The same was observed by Yamashita et al. [24] for the Y-Ni-Mg compound identified as 12R and described by them with a periodic structural model in the *R*32 space group with *a* = 22.4 and *c* = 33.1 Å. In the *a*-*b* plane, the proposed structure is a 7x superstructure with respect to *hcp*-Mg.

The 3D ED-based structure solution proposed here properly includes all these features and improves the description providing an ab initio model obtained without a priori assumptions on the structure.

From 3D ED, LPSO-5 has a constant stacking of slabs of 10.46(2) Å thickness in agreement with what is observed in HRTEM images. Within one slab, $Mg@Y_8Ni_6$ clusters are forming trimers periodically distributed (see Fig. 9) ensuring the same composition of all slabs. The

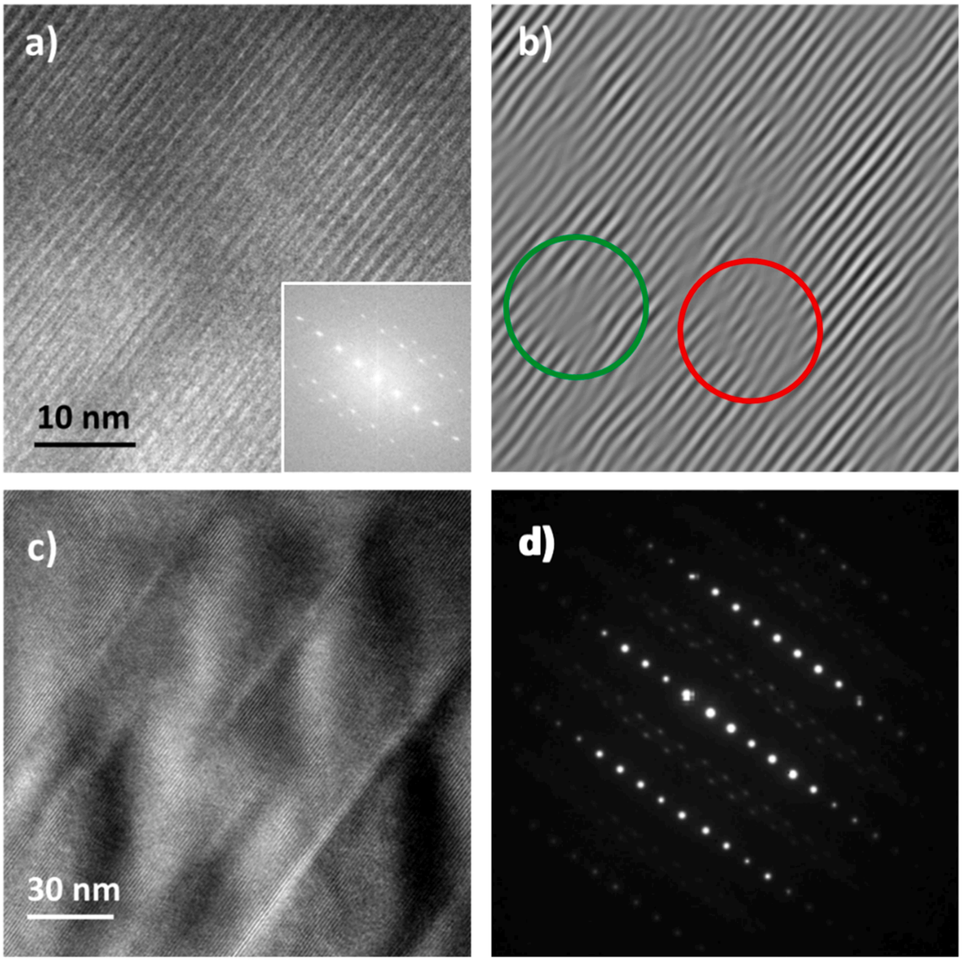

Fig. 8. Results of TEM characterization of LPSO-5. (a) HRTEM image close to [010] direction showing a layered structure with interplanar distance of about 10–11 Å. The related FFT, shown in the inset, reveals the presence of two weak lines of satellite reflections. (b) The same HRTEM image after filtering-in only the first order reflections at 10.4 Å, in order to emphasize the presence of defects. Closure of layers is marked with a green circle; kinking of layers is marked with a red circle. (c) HRTEM image at lower magnification showing stacking faults parallel to the layers. (d) SAED pattern showing the main lattice periodicity of about 10.4 Å, the second line of reflections at about 2.7 Å and, in-between, the lines with weak reflections and diffuse scattering coherent with 7x superstructure.

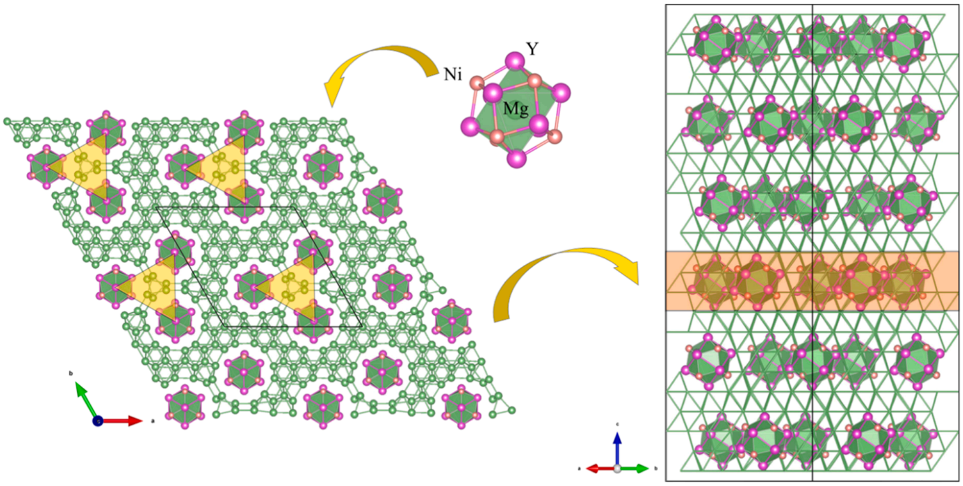

Fig. 9. LPSO-5 3D average model from a single Mg@Y_8Ni_6 cluster to the cluster distribution within each slab to the slabs stacking along c. Yellow triangles highlight the distribution of clusters within a slab; the orange rectangle highlights a slab in the crystal space.

modulation affects how the arrangement of trimers is shifted and rotated in the (a,b) plane from one layer to the next one (see Fig. S7). These tiny changes from slab to slab are the main difference between our model and that proposed by Yamashita et al [24]; from the electrostatic potential maps it was also definitely established that clusters are Mg-centered, in a complete agreement with compositional data obtained by EDXS.

3.3. Structural generalization of Y-Ni-Mg LPSO phases

Any crystallography or solid-state textbook begins with an explanation of pure metal crystal structures, the most common of which are built by different stackings of triangular compact layers, as in the *fcc* (adopted by Ni), *hcp* (adopted by Mg) and mixed variant (adopted by some rare earths) cases [58,59].

From the structural point of view, the compounds studied here are undoubtedly very complex and a simplified and unified description of these is as desirable as it is challenging. Nevertheless, the crystal structures of compounds under study can be conceptually derived from a simple Mg matrix. Let's imagine a hypothetical lattice made of compact layers of Mg atoms stacked in some way. At some positions within these layers Mg is replaced by Y and Ni atoms. Due to the different sizes of Y and Ni with respect to Mg, these do not occupy the exact positions of the compact layer, but are somewhat displaced, making each layer slightly corrugated. The three structures studied here can be built from such corrugated layers, stacked so that Y and Ni atoms form Mg@Y_8Ni_6 clusters, where the central Mg is interstitial/interlayer. These clusters are all the same, and each of them is embedded in four corrugated layers in all structures (see Fig. 3, Figs. 6 and Fig. 9). Depending on where each layer "cuts" the cluster, isolated Y atoms (apical positions 1 or 4) or groupings of 3Y/3Ni atoms (intermediate positions 2 or 3) may be found (Fig. 10). What differentiates the three phases is the distribution of these clusters in the Mg matrix-base, which is reflected in the composition and sequence of the layers.

In LPSO-8 ($Y_8Ni_6Mg_{19}$), all corrugated layers are identical, they contain both isolated Y atoms and 3Y/3Ni groups and are stacked in the *fcc* mode (see Fig. 11). It is interesting to emphasize the relation between the 2D representation of the stacking, suggesting a 12-layer periodicity, and the 3D unit cell, containing information about all symmetry elements and not only the translational ones. The compositional difference between the compound ($Y_8Ni_6Mg_{19}$) and layers ($Y_8Ni_6Mg_{18}$) is due to the presence of the interlayer Mg atoms in the centers of the clusters.

The distribution of Mg@Y_8Ni_6 clusters in both LPSO-6 and LPSO-5 is aperiodic, which is the origin of their modulated structures that we described in supercells derived from their 6D and 5D superspace representations, respectively. In LPSO-6, layers have different compositions and are of different types: some of them cut clusters in all four possible positions (see Fig. 12), others in different combinations (Fig. S8). This complexity, at a bigger scale, results in the abovementioned undulating rows of clusters. The stacking topology of layers along the diagonal of

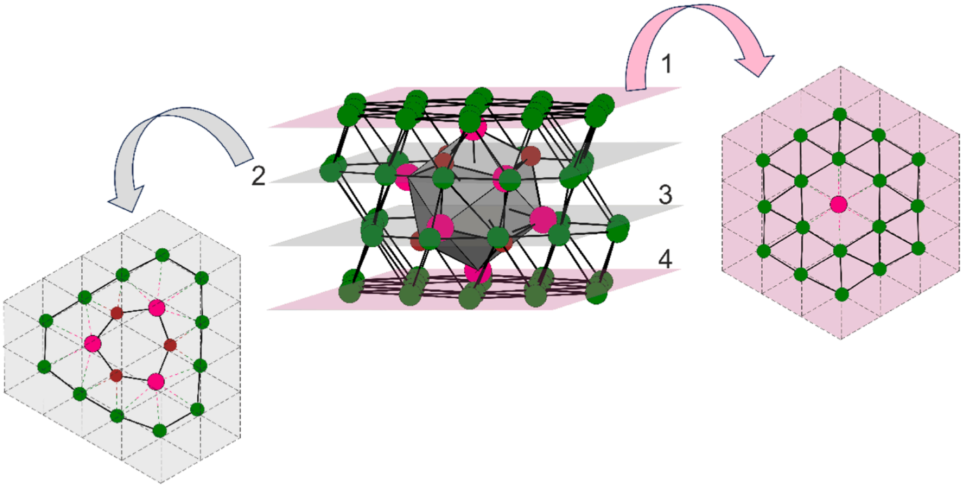

Fig. 10. Schematic representation of a single Mg@Y_8Ni_6 cluster embedded into the Mg matrix (central part); top views of layer 1 (pink background) and layer 2 (grey background). Black dotted lines serve as an eye guide, corresponding to an ideal compact layer.

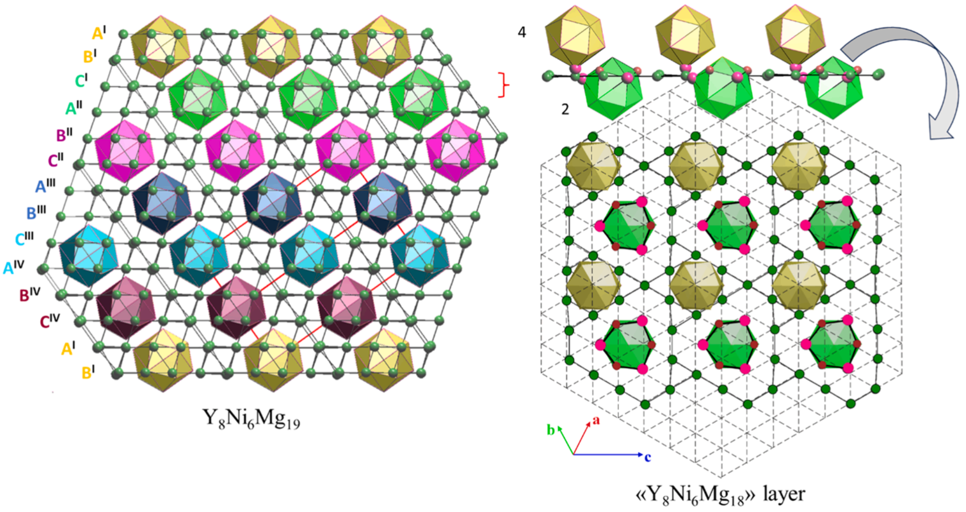

Fig. 11. The architecture of the LPSO-8 compound highlighting the Mg@Y_8Ni_6 clusters distribution (left). The cluster colouring scheme highlights their different positions in relation to the stacking direction. The unit cell edges are outlined in red. Side view of the cluster positions with respect to a single layer (right-upper part). Top view of a single corrugated layer (right-lower part).

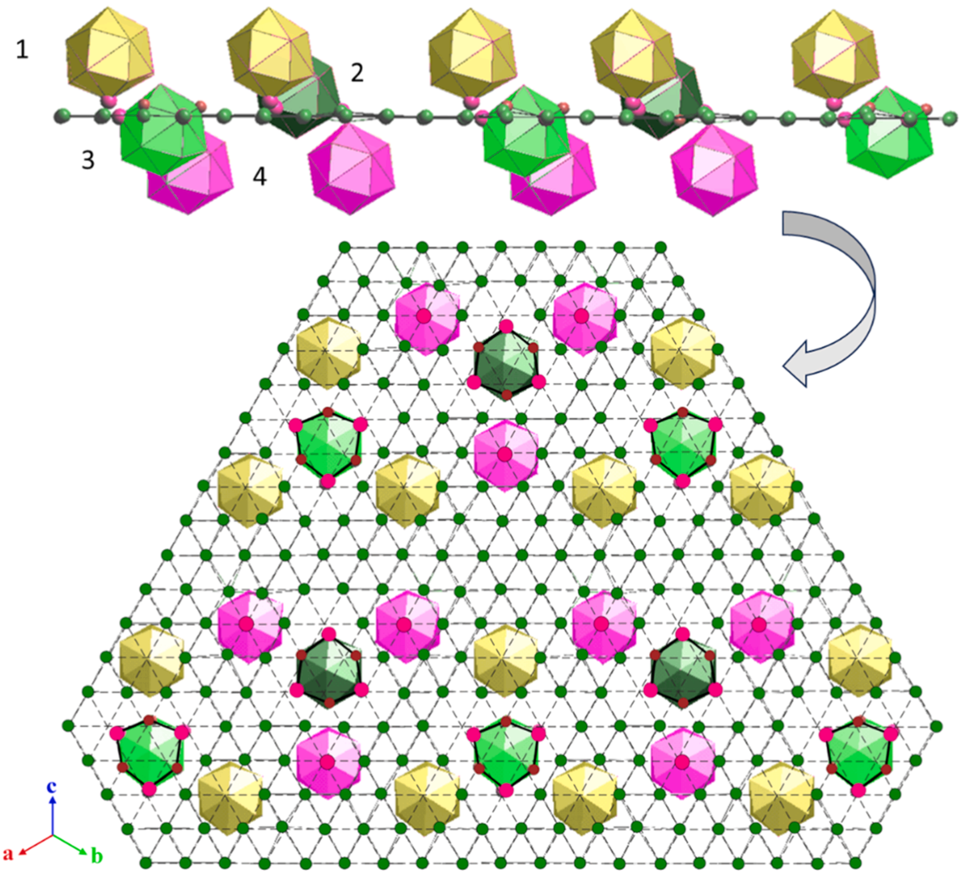

Fig. 12. A selected layer of the LPSO-6 compound (3D average model). Side view of Mg@Y_8Ni_6 clusters positions with respect to this layer (top). Top view where the relative heights of clusters are indicated by the same colouring scheme (bottom part).

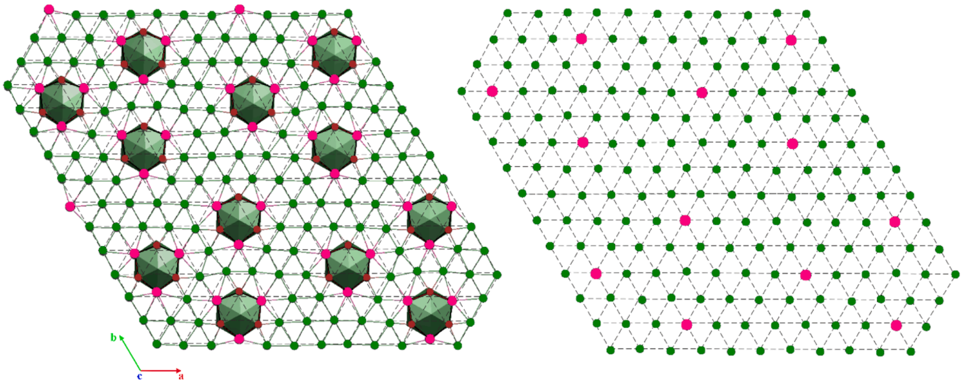

Fig. 13. Top view of the two types of layers of the LPSO-5 compound (average model). Layer containing only 3Y/3Ni groups (left); layer containing only isolated apical Y atoms (right).

the cubic cell is of the *fcc* type, as for LPSO-8.

In LPSO-5, layers of two different compositions, illustrated in Fig. 13, are stacked either in *fcc* or *hcp* mode, in such a way that each layer cuts all the clusters in the same position (1, 2, 3 or 4). The whole structure can be viewed as a stacking of four-layer thick slabs along the *c*-direction. This description of LPSO-5 is in line with that proposed by Yamashita et al [24] and can be naturally joined with that of the Mg-richer 10H, 18R and 14H LPSO compounds, traditionally viewed in terms of slabs containing Y/Ni clusters alternated with pure *hcp*-Mg fragments [16].

At this point, considering all the Y-Ni-Mg phases distributed along the Y/Ni=4/3 compositional line, it is clear that they belong to the same family, being all composed of Mg@Y_8Ni_6 clusters more or less densely distributed in a Mg matrix. Two subfamilies can be envisaged depending on the layer stacking mode (see Fig. 14). Using the Jagodzinski notation, they can be identified as:

1) *c*-type (corresponding to pure *fcc* stacking) adopted by LPSO-8 and LPSO-6, discovered here
2) *(h)$_n$cc*-type (corresponding to hybrid *fcc/hcp* stacking, $n \geq 2$), adopted by LPSO-5 ($n=2$), structurally elucidated in this work, and by Mg-richer representatives, extensively studied during the last decades. The *n* value increases with the Mg content, representing the pure *hcp*-

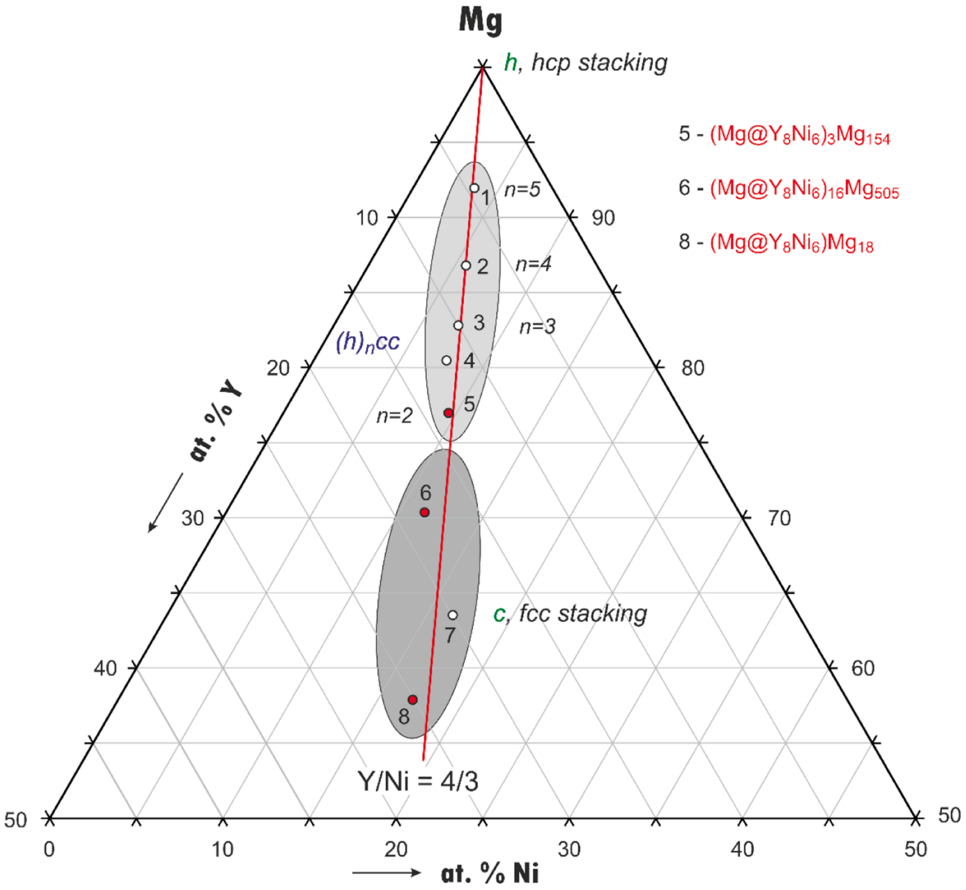

Fig. 14. Gibbs triangle showing the Y-Ni-Mg LPSO phases distributed between two sub-families according to the topology of the Mg matrix in terms of layer stacking, indicated by the Jagodzinski notation. For compounds studied here, formulas hinting the common structural principle of LPSO phases are indicated in red.

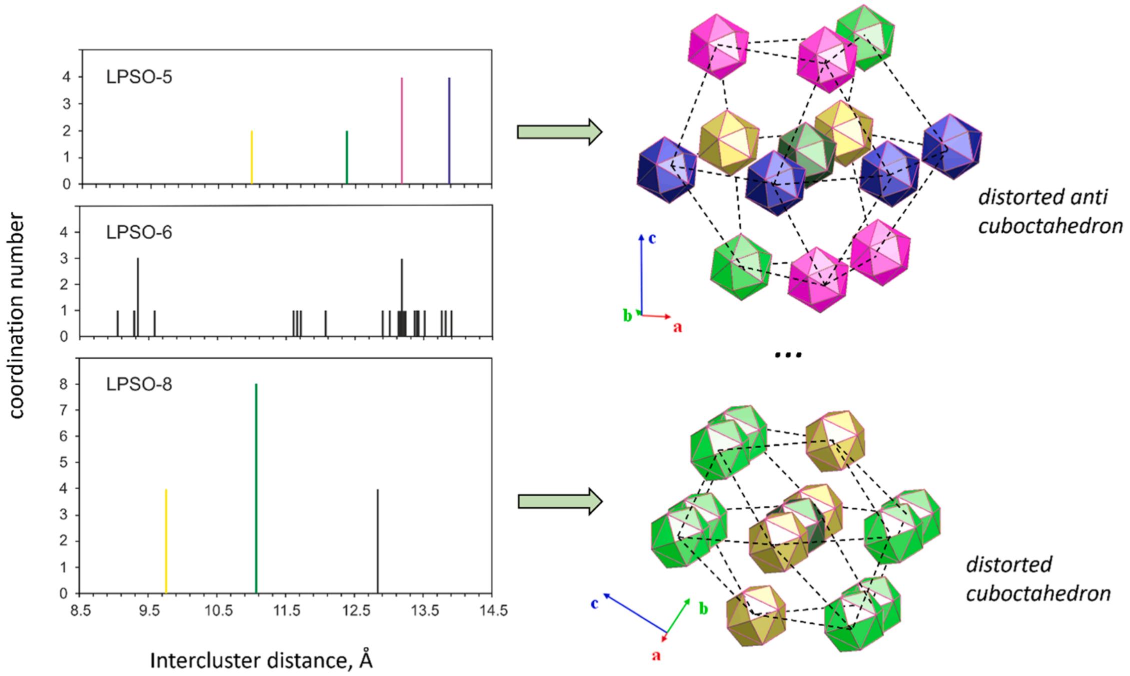

Fig. 15. Histograms of the distribution of intercluster distances in the studied compounds (left). First sphere coordination of clusters in LPSO-8 and LPSO-5 deriving from their *fcc* and *hcp* packing, respectively (right).

Mg slabs traditionally identified as an essential feature of LPSO phases [16].

The common architecture of LPSO phases can be highlighted by an unconventional formula indicating the ratio between Mg@Y_8Ni_6 clusters and the Mg atoms in the matrix, so reflecting their "dilution". For the compounds studied here such formulas are (Mg@Y_8Ni_6)Mg_{18} (LPSO-8), (Mg@Y_8Ni_6)$_{16}Mg_{505}$ (LPSO-6) and (Mg@Y_8Ni_6)$_3Mg_{154}$ (LPSO-5).

In all formulas the interstitial Mg centring clusters is also evidenced; this feature was experimentally, undoubtedly established for the first time in this work, confirming some theoretical findings in the similar Y-Zn-Mg system [60].

An analysis of intercluster distances helps to understand possible principles governing their dilution. Taking into account that the rhombododecahedron can be approximated by a sphere of about 3.7 Å radius and that no vertex sharing occurs, the minimum intercluster distance (from centre to centre) can be estimated to be around 9 Å. In fact, in the (Mg@Y_8Ni_6)Mg_{18} compound (LPSO-8), each cluster is coordinated by 12 neighbours in the form of a distorted cuboctahedron, distanced from the central one at 9.7 and 11 Å (see Fig. 15). So, the most compact *fcc* packing of clusters is realized in this compound, suggesting that it is the Mg-poorest endmember of the LPSO family.

When moving to the more diluted (Mg@Y_8Ni_6)$_{16}Mg_{505}$ (LPSO-6), the intercluster distances are similar, smearing out around the values ~9.3, 11.6 and 13 Å. Even if the average structure possesses an *fcc* Bravais lattice, a definite cluster coordination geometry is not identifiable, reflecting the complexity due to modulation.

Increasing further the Mg content, in the (Mg@Y_8Ni_6)$_3Mg_{154}$ (LPSO-5), clusters shift away a little from each other, being distanced at around 11, 12.5 and 13.5 Å. Here, each cluster is coordinated by 12 neighbours in the form of a distorted anti-cuboctahedron, typical of a *hcp* packing, marking the beginning of the *(h)$_n$cc*-type subfamily.

It is worth emphasizing that in the Mg-richer members LPSO-3 (10H), LPSO-2 (18R) and LPSO-1 (14H), the dilution of clusters has a somehow anisotropic character. They remain at similar distances inside slabs, which are more and more apart with the spaces filled by Mg.

A general trend can be inferred from the behaviour described above: the Mg@Y_8Ni_6 clusters are clearly the fundamental units for the formation and structures of LPSO phases. Increasing the magnesium content, these units have more degrees of freedom for their arrangement in the crystal structure. Nevertheless, they tend to form sorts of aggregates at characteristic distances, the distribution of which is at the origin of structural modulation, experimentally found in this work, and probably realized even in compounds not yet fully characterized.

Both the range of distances between clusters and their tendency to gather near each other agree with a previous DFT modelling work on similar Y_8T_6 (T = Zn, Al) nanocluster distribution in Mg-based alloys [61]: we believe that our experimental data could be a valuable input for further research on clusters assembly in LPSO-based materials.

4. Conclusions

The principal outcome of this work is the unprecedented structural elucidation of some Mg-based LPSO phases, achieved mainly thanks to the recently evolved 3D ED technique.

Modulated structures, completely described by super-space models, were naturally derived from experimental data, crossing the limits of classical electron diffraction approaches used for these materials, for which X-ray diffraction is not viable. Considering our findings, alloys and intermetallic compounds represent a fruitful field for 3D ED, contributing not only to exploitation but also to improving the electron crystallography science.

It is also worth underlining that suitable samples are an indispensable requirement for a successful application of any experimental method, and, in this case, these were obtained thanks to the knowledge gained through a systematic ten-year work on Y-Ni-Mg phase equilibria.

The validity of the obtained structural models is also confirmed by their excellent agreement with compositions measured by EDXS, which is extremely important for the identification of compounds in densely populated LPSO-forming systems. Furthermore, one of the main factors contributing to the previous composition discrepancies is the presence of interlayer Mg, centring the Y_8Ni_6 units, impossible to detect without complete 3D ED datasets. Based on these achievements, we suggest that this structural feature is always the same for other Y-Ni-Mg LPSO phases, leading to a new definition of them, probably extendable to other systems: *Mg-based LPSO phases contain Mg@Y_8Ni_6 clusters embedded in a magnesium matrix with fcc (c-type) or hybrid fcc/hcp ((h)$_n$cc-type) layer stacking modes.*

The *fcc* subfamily was discovered in this work, and its Mg-poorer end-member corresponds to (Mg@Y_8Ni_6)Mg_{18} (57.5 at % Mg), where the closest cluster packing is realized. To our conviction, the existence of analogous compounds in other systems could be a hint for further discovery of new *fcc*-type LPSO phases.

Compositions of the Y-Ni-Mg samples prepared; SEM Microphotographs (BSE mode) and results of phase analysis; HAADF-STEM images of extracted lamellae; 3D electrostatic potential maps and Camel plots for LPSO-6 and LPSO-5; selected layers of LPSO-6; atomic coordinates and equivalent displacement parameters for LPSO-8, LPSO-6 and LPSO-5 (commensurate three-dimensional average models). X-ray crystallographic files in CIF format.

CRediT authorship contribution statement

Pavlo Solokha: Writing – review & editing, Writing – original draft, Visualization, Validation, Supervision, Methodology, Investigation, Formal analysis, Conceptualization. **Riccardo Freccero:** Writing – review & editing, Investigation. **Mauro Gemmi:** Investigation. **Iryna Andrusenko:** Investigation, Formal analysis. **Paola Parlanti:** Investigation. **Enrico Mugnaioli:** Investigation, Formal analysis. **Gwladys Steciuk:** Writing – original draft, Visualization, Formal analysis. **Lukas Palatinus:** Writing – review & editing. **Serena De Negri:** Writing – review & editing, Writing – original draft, Validation, Supervision, Methodology, Investigation, Conceptualization.

Declaration of competing interest

The authors declare that they have no known competing financial interests or personal relationships that could have appeared to influence the work reported in this paper.

Supplementary materials

Supplementary material associated with this article can be found, in the online version, at doi:10.1016/j.actamat.2025.121279.

References

[1] J. Song, J. Chen, X. Xiong, X. Peng, D. Chen, F. Pan, Research advances of magnesium and magnesium alloys worldwide in 2021, J. Magnes. Alloy. 10 (2022) 863–898, https://doi.org/10.1016/j.jma.2022.04.001.

[2] E. Abe, Y. Kawamura, K. Hayashi, A. Inoue, Long-period ordered structure in a high-strength nanocrystalline Mg-1 At % Zn-2 At % Y alloy studied by atomic-resolution Z-contrast STEM, Acta Mater. 50 (15) (2002) 3845–3857, https://doi.org/10.1016/S1359-6454(02)00191-X.

[3] D. Xu, E.H. Han, Y. Xu, Effect of long-period stacking ordered phase on microstructure, mechanical property and corrosion resistance of Mg alloys: A review, Prog. Nat. Sci. Mater. Int. 26 (2) (2016) 117–128, https://doi.org/10.1016/J.PNSC.2016.03.006.

[4] H. Liu, H.E. Huang, C.E. Wang, J. Sun, J. Bai, F. Xue, A. Ma, X.-B. Chen, Recent advances in LPSO-containing wrought magnesium alloys: relationships between processing, microstructure, and mechanical properties, JOM, 71 (9) (2019) 3314–3327, https://doi.org/10.1007/s11837-019-03610-9.

[5] A.A. Kaya, A review on developments in magnesium alloys, Front. Mater. 7 (2020) 484613, https://doi.org/10.3389/FMATS.2020.00198/BIBTEX.

[6] Y. Nie, J. Dai, X. Li, X. Zhang, Recent developments on corrosion behaviors of Mg alloys with stacking fault or long period stacking ordered structures, J. Magnes. Alloy. 9 (4) (2021) 1123–1146, https://doi.org/10.1016/J.JMA.2020.09.021.

[7] Geshani, M.S.; Kalayeh, P.M.; Asadi, A.H.; Mirzadeh, H.; Malekan, M.; Emamy, M. A review of Mg alloys containing long-period stacking ordered (LPSO) structures with insight into the application of friction stir processing. 2023. https://doi.org/10.1016/j.jmrt.2023.04.105.

[8] T. Itoi, K. Takahashi, H. Moriyama, M. Hirohashi, A high-strength Mg–Ni–Y alloy sheet with a long-period ordered phase prepared by hot-rolling, Scr. Mater. 59 (10) (2008) 1155–1158, https://doi.org/10.1016/J.SCRIPTAMAT.2008.08.001.

[9] Tong, L.B.; Li, X.H.; Zhang, H.J. Effect of long period stacking ordered phase on the microstructure, texture and mechanical properties of extruded Mg-Y-Zn alloy. 2012. https://doi.org/10.1016/j.msea.2012.10.088.

[10] S.M. Zhu, R. Lapovok, J.F. Nie, Y. Estrin, S.N. Mathaudhu, Microstructure and mechanical properties of LPSO phase dominant Mg$_{85.8}$Y$_{7.1}$Zn$_{7.1}$ and Mg$_{85.8}$Y$_{7.1}$Ni$_{7.1}$ alloys, Mater. Sci. Eng. A 692 (2017) 35–42, https://doi.org/10.1016/J.MSEA.2017.03.057.

[11] J. Wang, S. Gao, X. Liu, X. Peng, K. Wang, S. Liu, W. Jiang, S. Guo, F. Pan, Enhanced mechanical properties and degradation rate of Mg-Ni-Y alloy by introducing LPSO phase for degradable fracturing ball applications, J. Magnes. Alloy. 8 (2020) 127–133, https://doi.org/10.1016/j.jma.2019.11.010.

[12] S.Z. Wu, X.G. Qiao, S.H. Qin, Y.Q. Chi, M.Y. Zheng, Improved strength in wrought Mg-Y-Ni alloys by adjusting the block-shaped LPSO phase and plate-shaped γ' phase, Mater. Sci. Eng. A 831 (2022) 142198, https://doi.org/10.1016/j.msea.2021.142198.

[13] Wang, J.; Zhu, G.; Wang, L.; Zhang, X.; Knezevic, M.; Zeng, X. Strengthening mechanisms, hardening/softening behavior, and microstructure evolution in an LPSO magnesium alloy at elevated temperatures. 2023. https://doi.org/10.1016/j.matchar.2023.113066.

[14] A. Hossein Asadi, P. Mahmoud Kalayeh, H. Mirzadeh, M. Malekan, M. Emamy, Precipitation kinetics and mechanical properties of Mg-Y-Zn and Mg-Y-Ni alloys containing long-period stacking ordered (LPSO) structures, J. Mater. Res. Technol. 24 (2023) 9513–9522, https://doi.org/10.1016/j.jmrt.2023.05.159.

[15] *Scopus database*. https://www.scopus.com.

[16] Abe, E.; Ono, A.; Itoi, T.; Yamasaki, M.; Kawamura, Y. Polytypes of long-period stacking structures synchronized with chemical order in a dilute Mg–Zn–Y alloy. 2011, 91 (10), 690–696. https://doi.org/10.1080/09500839.2011.609149.

[17] K. Kishida, H. Yokobayashi, H. Inui, M. Yamasaki, Y. Kawamura, The crystal structure of the LPSO phase of the 14H-type in the Mg–Al–Gd alloy system, Intermetallics 31 (2012) 55–64, https://doi.org/10.1016/J.INTERMET.2012.06.010.

[18] D. Egusa, E. Abe, The structure of long period stacking/order Mg-Zn-RE phases with extended non-stoichiometry ranges, Acta Mater. 60 (2012) 166–178, https://doi.org/10.1016/j.actamat.2011.09.030.

[19] M. Yamasaki, M. Matsushita, K. Hagihara, H. Izuno, E. Abe, Y. Kawamura, Highly ordered 10H-type long-period stacking order phase in a Mg–Zn–Y ternary alloy, Scr. Mater. 78–79 (2014) 13–16, https://doi.org/10.1016/J.SCRIPTAMAT.2014.01.013.

[20] P. Krishna, D. Pandey, Close-Packed Structures, University College Cardiff Press, Cardiff, 1981.

[21] D. Zagorac, H. Müller, S. Ruehl, J. Zagorac, S. Rehme, Recent developments in the inorganic crystal structure database: theoretical crystal structure data and related features, J. Appl. Cryst 52 (2019) 918–925, https://doi.org/10.1107/S160057671900997X.

[22] P. Villars, K. C. Pearson's Crystal Data: crystal Structure Database for inorganic compounds, release 2021/2022. ASM International, Materials Park, Ohio, USA.

[23] H. Yokobayashi, K. Kishida, H. Inui, M. Yamasaki, Y. Kawamura, Enrichment of Gd and Al atoms in the quadruple close packed planes and their In-plane long-range ordering in the long period stacking-ordered phase in the Mg-Al-Gd system, Acta Mater. 59 (19) (2011) 7287–7299, https://doi.org/10.1016/j.actamat.2011.08.011.

[24] K. Yamashita, T. Itoi, M. Yamasaki, Y. Kawamura, E. Abe, A novel long-period stacking/order structure in Mg-Ni-Y alloys, J. Alloys Compd. 788 (2019) 277–282, https://doi.org/10.1016/J.JALLCOM.2019.02.219.

[25] M. Gemmi, E. Mugnaioli, T.E. Gorelik, U. Kolb, L. Palatinus, P. Boullay, S. Hovmöller, J.P. Abrahams, 3D Electron diffraction: the nanocrystallography revolution, ACS Cent. Sci. 5 (8) (2019) 1315, https://doi.org/10.1021/ACSCENTSCI.9B00394.

[26] A. Stewart, U. Kolb, Introduction to three dimensional electron crystallography, Encycl. Mater. Tech. Ceram. Glas. 1–3 (2021) 618–633, https://doi.org/10.1016/B978-0-12-818542-1.00097-7.

[27] E. Mugnaioli, M. Gemmi, Single-crystal analysis of nanodomains by electron diffraction tomography: mineralogy at the order-disorder borderline, Zeitschrift fur Krist. - Cryst. Mater. 233 (3–4) (2018) 163–178, https://doi.org/10.1515/ZKRI-2017-2130/ASSET/GRAPHIC/J_ZKRI-2017-2130_FIG_007.JPG.

[28] I. Andrusenko, V. Hamilton, E. Mugnaioli, A. Lanza, C. Hall, J. Potticary, S.R. Hall, M. Gemmi, The crystal structure of orthocetamol solved by 3D electron diffraction, Angew. Chemie 131 (32) (2019) 11035–11038, https://doi.org/10.1002/ANGE.201904564.

[29] J. Plášil, G. Steciuk, J. Majzlan, R. Škoda, J. Filip, M. Petr, J. Kolařík, M. Klementová, O. Bähre, G. Klöß, L. Lapčák, 3D Electron diffraction as a powerful tool to study the earliest nanocrystalline weathering products: A case study of uraninite weathering, ACS Earth Sp. Chem. 40 (2021) 34, https://doi.org/10.1021/ACSEARTHSPACECHEM.1C00386/SUPPL_FILE/SP1C00386_SI_002.CIF.

[30] I. Andrusenko, M. Gemmi, 3D Electron diffraction for structure determination of small-molecule nanocrystals: A possible breakthrough for the pharmaceutical industry, Wiley Interdiscip. Rev. Nanomedicine Nanobiotechnology 14 (5) (2022) e1810, https://doi.org/10.1002/WNAN.1810.

[31] C.A. Corrêa, O. Perez, J. Kopeček, P. Brázda, M. Klementová, L. Palatinus, Crystal structures of H″-Cu$_{3+x}$Si and H‴-Cu$_{3+x}$Si, Acta Crystallogr. Sect. B Struct. Sci. Cryst. Eng. Mater. 73 (4) (2017) 767–774, https://doi.org/10.1107/S2052520617006163/BP5097ETA2SUP3.HKL.

[32] S. Samuha, E. Mugnaioli, B. Grushko, U. Kolb, L. Meshi, Atomic structure solution of the complex quasicrystal approximant Al$_{77}$Rh$_{15}$Ru$_{8}$ from electron diffraction data, Acta Crystallogr. Sect. B Struct. Sci. Cryst. Eng. Mater. 70 (6) (2014) 999–1005, https://doi.org/10.1107/S2052520614022033/WF5113ISUP2.HKL.

[33] D. Singh, Y. Yun, W. Wan, B. Grushko, X. Zou, S. Hovmöller, A complex pseudo-decagonal quasicrystal approximant, Al$_{37}$(Co,Ni)$_{15.5}$, solved by rotation electron diffraction, J. Appl. Crystallogr. 47 (1) (2014) 215–221, https://doi.org/10.1107/S1600576713029294/HE5621SUP3.PDF.

[34] L. Gu, N. Wang, X. Tang, H.G. Changela, Application of FIB-SEM techniques for the advanced characterization of Earth and planetary materials, Scanning 2020 (2020), https://doi.org/10.1155/2020/8406917.

[35] V.V. Shtender, V.V. Pavlyuk, G.S. Dmytriv, W. Nitek, W. Łasocha, G. Cichowicz, M. K. Cyrański, V. Paul-Boncour, I.Y. Zavaliy, Synthesis and crystal structure of new compounds from the Y–Mg–Ni system, Zeitschrift für Krist. - Cryst. Mater. 234 (1) (2019) 19–32, https://doi.org/10.1515/zkri-2018-2107.

[36] Bruker, APEX4 V2022.10-0, Bruker AXS Inc., Madison, Wisconsin, USA, 2022.

[37] G.M. Sheldrick, SHELXL-2019/1, Bruker AXS Inc., Madison, Wisconsin, USA, 2019.

[38] Rasband, W.S. ImageJ. U. S. National Institutes of Health: Bethesda, Maryland, USA. https://imagej.net/ij/.

[39] A. Lanza, E. Margheritis, E. Mugnaioli, V. Cappello, G. Garau, M. Gemmi, Nanobeam precession-assisted 3D electron diffraction reveals a new polymorph of hen egg-white lysozyme, IUCrJ 6 (2) (2019) 178–188, https://doi.org/10.1107/S2052252518017657/EH5001SUP1.PDF.

[40] I. Nederlof, E. Van Genderen, Y.W. Li, J.P. Abrahams, A Medipix Quantum area detector allows rotation electron diffraction data collection from submicrometre three-dimensional protein crystals, Acta Cryst D69 (7) (2013) 1223–1230, https://doi.org/10.1107/S0907444913009700.

[41] R. Vincent, P.A. Midgley, Double conical beam-rocking system for measurement of integrated electron diffraction intensities, Ultramicroscopy 53 (3) (1994) 271–282.

[42] M. Gemmi, M.G.I. La Placa, A.S. Galanis, E.F. Rauch, S. Nicolopoulos, Fast electron diffraction tomography, J. Appl. Crystallogr. 48 (3) (2015) 718–727, https://doi.org/10.1107/S1600576715004604/KS5462ISUP2.HKL.

[43] L. Palatinus, P. Brázda, M. Jelínek, J. Hrdá, G. Steciuk, M. Klementová, Specifics of the data processing of precession electron diffraction tomography data and their implementation in the program PETS2.0, Acta Crystallogr. Sect. B Struct. Sci. Cryst. Eng. Mater. 75 (2019) 512–522, https://doi.org/10.1107/S2052520619007534.

[44] P. Brázda, M. Klementová, Y. Krysiak, L. Palatinus, Accurate lattice parameters from 3D electron diffraction data. I. Optical distortions, IUCrJ 9 (6) (2022) 1–21, https://doi.org/10.1107/s2052252522007904.

[45] Khouchen, M.; Klar, B.; Chintakindi, H. Optimal estimated standard uncertainties of reflection intensities for kinematical refinement from 3D electron diffraction data research papers. 2023, 1–13. https://doi.org/10.1107/S2053273323005053.

[46] Q.Q. Jin, C.F. Fang, S.B. Mi, Formation of long-period stacking ordered structures in Mg$_{88}$M$_{5}$Y$_{7}$ (M = Ti, Ni and Pb) casting alloys, J. Alloys Compd. 568 (2013) 21–25, https://doi.org/10.1016/J.JALLCOM.2013.03.061.

[47] C. Liu, Y. Zhu, Q. Luo, B. Liu, Q. Gu, Q. Li, A 12R long-period stacking-ordered structure in a Mg-Ni-Y alloy, J. Mater. Sci. Technol. 34 (12) (2018) 2235–2239, https://doi.org/10.1016/J.JMST.2018.06.015.

[48] M. Mezbahul-Islam, D. Kevorkov, M. Medraj, M. Mezbahul-Islam, D. Kevorkov, M. Medraj, Experimental study of the Mg-Ni-Y system at 673 K using diffusion couples and key alloys, Metals (Basel) 5 (3) (2015) 1746–1769, https://doi.org/10.3390/met5031746.

[49] M. Jiang, S. Zhang, Y. Bi, H. Li, Y. Ren, G. Qin, Phase equilibria of the long-period stacking ordered Phase in the Mg–Ni–Y system, Intermetallics 57 (2015) 127–132, https://doi.org/10.1016/J.INTERMET.2014.10.014.

[50] K. Xu, S. Liu, D. Huang, Y. Du, Experimental investigation of the isothermal section of the Mg–Ni–Y system with LPSO phases at 400°C, J. Mater. Sci. 53 (12) (2018) 9243–9257, https://doi.org/10.1007/s10853-018-2192-9.

[51] M. Mezbahul-Islam, M. Medraj, A critical thermodynamic assessment of the Mg-Ni, Ni-Y binary and Mg-Ni-Y ternary systems, CALPHAD Comput. Coupling Phase Diagrams\penalty \z@ \protect \futurelet \@let@token Thermochem 33 (2009) 478–486, https://doi.org/10.1016/j.calphad.2009.01.001.

[52] Z. Wang, Q. Luo, S. Chen, K.C. Chou, Q. Li, Experimental investigation and thermodynamic calculation of the Mg-Ni-Y system (Y < 50 at. %) at 400 and 500°C, J. Alloys Compd. 649 (2015) 1306–1314, https://doi.org/10.1016/J.JALLCOM.2015.07.202.

[53] S. Linsinger, U.C. Rodewald, R. Pöttgen, Nd4.67Ru3Mg8.83 – A magnesium-rich compound with Ru@Mg4Nd4 square antiprisms and Mg@Mg8 cubes as -basic building units, Zeitschrift für Anorg. und Allg. Chemie 638 (10) (2012) 1457–1461, https://doi.org/10.1002/ZAAC.201200124.

[54] S. Stein, M. Kersting, L. Heletta, R. Pöttgen, Rare earth-ruthenium-magnesium intermetallics, Zeitschrift fur Naturforsch. - Sect. B J. Chem. Sci. 72 (6) (2017) 447–455, https://doi.org/10.1515/ZNB-2017-0048.

[55] L. Palatinus, G. Chapuis, SUPERFLIP - A computer program for the solution of crystal structures by charge flipping in arbitrary dimensions, J. Appl. Crystallogr. 40 (4) (2007) 786–790, https://doi.org/10.1107/S0021889807029238.

[56] L. Palatinus, The charge-flipping algorithm in crystallography, Acta Crystallogr. Sect. B Struct. Sci. Cryst. Eng. Mater. 69 (1) (2013) 1–16, https://doi.org/10.1107/S2052519212051366.

[57] S. Van Smaalen, IUCr Monographs On Crystallography - 21 - Incommensurate Crystallography, Oxford Univ. Press Inc., New York, 2007, p. 283.

[58] U. Müller, Inorganic Structural Chemistry, John Wiley & Sons, Ltd: Chichester, UK, 2006, https://doi.org/10.1002/9780470057278.

[59] W. Steurer, Crystal structures of metallic elements and compounds, Phys. Metall. Fifth Ed. 1 (2014) 1–101, https://doi.org/10.1016/B978-0-444-53770-6.00001-0.

[60] M. Itakura, M. Yamaguchi, D. Egusa, E. Abe, Density functional theory study of Solute cluster growth processes in Mg-Y-Zn LPSO alloys, Acta Mater. 203 (2021) 116491, https://doi.org/10.1016/J.ACTAMAT.2020.116491.

[61] H. Kimizuka, S. Kurokawa, A. Yamaguchi, A. Sakai, S. Ogata, Two-dimensional ordering of solute nanoclusters at a close-packed stacking fault: modeling and experimental analysis, Sci. Reports 4 (1) (2014) 1–12, https://doi.org/10.1038/srep07318. *2014 41*.